

# Binary black holes population and cosmology in new lights: Signature of PISN mass and formation channel in GWTC-3

Christos Karathanasis<sup>1†</sup>, Suvodip Mukherjee<sup>2‡</sup>, Simone Mastrogiovanni<sup>3,4§</sup>

<sup>1</sup> *Institut de Física d'Altes Energies (IFAE), Barcelona Institute of Science and Technology, Barcelona, Spain*

<sup>2</sup> *Perimeter Institute for Theoretical Physics, 31 Caroline Street N., Waterloo, Ontario, N2L 2Y5, Canada*

<sup>3</sup> *Artemis, Université Côte d'Azur, Observatoire de la Côte d'Azur, CNRS, F-06304 Nice, France*

2 May 2022

## ABSTRACT

The mass, spin, and merger rate distribution of the binary black holes (BBHs) across cosmic redshifts provide a unique way to shed light on their formation channel. Along with the redshift dependence of the BBH merger rate, the mass distribution of BBHs can also exhibit redshift dependence due to different formation channels and due to its dependence on the metallicity of the parent stars. In this work, we explore the redshift dependence of the BBH mass distribution jointly with the merger rate evolution from the third gravitational wave (GW) catalog GWTC-3 of the LIGO-Virgo-KAGRA collaboration. This analysis sheds light on multiple new aspects of the BBH formation channel and mass distribution. We obtain interesting constraints on the minimum delay time between the formation of stars and mergers of BBHs  $t_d^{\min} = 1.95_{-0.93}^{+0.97}$  Gyrs, along with a hint towards a steeper power-law form of the delay time distribution  $((t_d)^d)$  with an index  $d < -1.55$  at 68% C.L. The mass distribution of the BBHs agrees with a power-law form with a Gaussian peak at  $\mu_g = 40.26_{-2.32}^{+1.04} M_\odot$  which agrees with the theoretical prediction of the lower edge of the PISN mass scale and differs from the previous analysis. This analysis sheds light on the lower edge of the PISN mass scale of black holes and provides hints toward the formation channel of the BBH systems that are different from the usual fiducial scenario with a power-law index  $d = -1$ . Our results are consistent with the scenarios of varying (or fixed) Hubble constant and also for events with lower matched filtering network signal to noise ratio.

**Key words:** gravitational waves, black hole mergers, cosmology: miscellaneous

## 1 INTRODUCTION

Gravitational wave (GW) observations bring a wealth of information to a broad range of topics ranging from astrophysics, cosmology, and fundamental physics. The first GW detection (Abbott et al. 2016b) opened a new way of observing the Universe. The latest measurements from the LIGO-Virgo-KAGRA (LVK) (Aasi et al. 2015; Abbott et al. 2016a, 2021a; Acernese et al. 2014; Aso et al. 2013; Gregory 2010; Tse et al. 2019; Abbott et al. 2018; Akutsu et al. 2020) have detected 90 compact objects which constituents of binary neutron stars (BNSs), neutron star binary black holes (NS-BHs), and binary black holes (BBHs) (Abbott et al. 2021b). The observed GW sources give a direct probe to infer the mass distribution of the compact objects across a range of cosmic redshifts. The recent measurement by the LVK collaboration exhibit that the mass distribution of the BBHs shows a power-law+Gaussian distribution (Abbott et al. 2021d,b,c; Virgo & Kagra 2021; Abbott et al. 2019b). Along with the mass distribution, a power-law model of the BBHs merger

rate is inferred from LVK analysis (Abbott et al. 2021d,b,c, 2019a, 2021f). The mass distribution of GW sources and the merger rate provides a direct way to understand the formation channel of BHs.

However, the mass distribution of the astrophysical BBHs is likely to exhibit a redshift dependence due to the dependence of the black hole masses on stellar properties, such as the stellar metallicity (Bethe & Brown 1998; Portegies Zwart & Yungelson 1998; Heger & Woosley 2002; Belczynski et al. 2002; Dominik et al. 2012; Dominik et al. 2015; Mapelli et al. 2017; Spera & Mapelli 2017; Giacobbo et al. 2018; Toffano et al. 2019; Farmer et al. 2019; Renzo et al. 2020; Mehta et al. 2022). As the BBHs merger happens after some delay time since its formation, this causes mixing between different black hole masses in the observed distribution. The mixing between different BHs will lead to mergers of BHs formed at different cosmic times (Mukherjee 2021). So, if the BHs were formed at different cosmic times, and consequently have different mass distribution, then the mixing of BBHs will also exhibit a redshift dependence. The redshift dependence of the BBHs will depend on the evolution of the stellar metallicity, the dependence of the black hole masses on the stellar metallicity, and on the delay time distribution of the BHs. Along with the

† ckarathanasis@ifae.es

‡ smukherjee1@perimeterinstitute.ca

§ simone.mastrogiovanni@oca.eu

mass distribution, the delay time distribution will also show up as a unique signature on the redshift dependence of the merger rate of BBHs. As a result, by exploring the merger rate of BBHs and their mass distribution, we can infer the delay time distribution of the binaries and also shed light on the dependence on stellar metallicity.

The mass distribution of the BBHs can also play an important role in inferring the cosmic expansion history (Taylor et al. 2012; Farr et al. 2019; Mastrogiovanni et al. 2021a; You et al. 2021; Mancarella et al. 2021; Mukherjee 2021; Leyde et al. 2022; Ezquiaga & Holz 2022). As the masses of the GW sources are redshifted ( $m^{\text{det}} = (1+z)m$ ), one can expect to infer the redshift from the mass distribution of the GW sources, if the mass distribution of the BBHs can exhibit a universal property or at least a standardized behavior. We can break the mass-redshift degeneracy and infer the cosmic expansion history from dark standard sirens without applying the cross-correlation technique (Oguri 2016; Mukherjee & Wandelt 2018; Mukherjee et al. 2020, 2021a; Bera et al. 2020; Scelfo et al. 2020; Mukherjee et al. 2021b; Cañas-Herrera et al. 2021; Scelfo et al. 2022; Cigarrán Díaz & Mukherjee 2022; Mukherjee et al. 2022) or statistical host identification technique (Schutz 1986; MacLeod & Hogan 2008; Del Pozzo 2012; Arabsalmani et al. 2013; Gray et al. 2020; Fishbach et al. 2019; Abbott et al. 2021e; Soares-Santos et al. 2019; Finke et al. 2021; Abbott et al. 2020b; Palmese et al. 2021). However, if BBHs mass distribution exhibits redshift dependence due to its intrinsic dependence on the delay time distribution, then cosmic redshifts cannot be accurately inferred (Mukherjee 2021; Ezquiaga & Holz 2022), and it can bias the results if the redshift dependence of the mass distribution is not considered. Exploring the merger rate distribution to explore cosmology from dark sirens is also studied for the third generation GW detectors (Ding et al. 2019; Ye & Fishbach 2021; Leandro et al. 2022).

In this paper, we make a first joint estimation of the BBH merger rate evolution, mass distribution, and cosmic expansion history allowing for the redshift dependence of the BBH mass distribution. This measurement makes it possible to also infer the delay time distribution of the BBHs in a consistent framework along with the cosmological parameters. The paper is organized as follows, In Sec. 2 we discuss the redshift dependence of the mass distribution of the BBHs and its merger rate. In Sec. 3 and Sec. 4 we discuss the basic Bayesian framework used in this analysis and we discuss the results from the joint estimation and compare these results with the results inferred by the LVK collaboration. Finally, we conclude the analysis of this work and future prospects in Sec. 5.

## 2 MODELLING REDSHIFT DEPENDENCE OF THE BLACK HOLE MASS DISTRIBUTION

The redshift dependence of the observed BBH mass distribution, that we consider in this analysis, is due to three effects, (i) metallicity dependence of the PISN mass scale, (ii) redshift dependence of the stellar metallicity, (iii) non-zero value of the delay time between the formation of the stars that will later become BHs, and for them to merge with another black hole. We will briefly describe below all these aspects.

(i) According to the pair-instability supernovae (PISN)

process, the mass distribution of BHs is expected to feature a mass gap due to the mass loss of heavy stars (Spera & Mapelli 2017; Farmer et al. 2019; Renzo et al. 2020). The mass loss during the PISN sets the lower limit of the mass gap at around  $M_{\text{PISN}} = 45 M_{\odot}$ . However,  $M_{\text{PISN}}$  is also closely related to the stellar metallicity. It was shown (Spera & Mapelli 2017; Farmer et al. 2019; Renzo et al. 2020) that  $M_{\text{PISN}}$  varies less than 10% for a variation of the stellar metallicity  $Z$  from  $10^{-5}$  to  $3 \times 10^{-3}$ . The stars with higher metallicity have a larger mass loss due to stellar winds, which leads to a lower value of the PISN mass scale, than stars formed with lower metallicity. As a result, the position of the  $M_{\text{PISN}}$  will vary.

(ii) The metallicity in the Universe varies with redshift and also with the individual galaxies. The global evolution of the stellar metallicity (Belczynski et al. 2002; Dominik et al. 2012; Dominik et al. 2015; Mapelli et al. 2017; Giacobbo et al. 2018; Safarzadeh & Farr 2019; Toffano et al. 2019) indicates that the Universe at high redshift has poor stellar metallicity than at low redshift. As a result, the BHs formed at high redshift may have a higher PISN mass scale than the BHs formed at low.

(iii) Finally, the BHs which we observe using GW, are not the individual BHs, but binaries. Though the formation of a black hole takes only a few Myrs, a black hole requires much more time to form a binary and merge. As a result, there is a non-zero delay time between the formation of a star and the merging of BHs. This delay time depends on the formation channels of the BBHs (O’Shaughnessy et al. 2010; Banerjee et al. 2010; Dominik et al. 2012; Dominik et al. 2015; Mandel & de Mink 2016; Lamberts et al. 2016; Cao et al. 2018; Elbert et al. 2018; Eldridge et al. 2019; Vitale et al. 2019; du Buisson et al. 2020; Santoliquido et al. 2021). Moreover, the delay time is not a fixed number for all the BHs, but rather it follows a distribution that is expected to be a power law from simulations. For a flat in the log-space distribution of the separation of the BHs, the delay time distribution is going to be  $t_d^{-1}$  with a minimum delay time from a few hundreds of Myrs to a few Gyrs, depending on the formation channels. The current constraints from GWTC-2 (Fishbach & Kalogera 2021) and the stochastic GW background (Mukherjee & Silk 2021) are weak. In the future, data-driven measurement is possible by combining GW sources with emission line signal (Mukherjee & Dizgah 2021).

Consequently, by combining these three effects, we can expect that the observed BHs detected in a binary system are going to have a redshift-dependent mass distribution. Following the analysis that was presented in Mukherjee (2021) the mass distribution of BHs at a merging redshift  $z_m$  is given by

$$P[m(z_m)] = P_s[m(z_m)]W_{t_d}[m(z_m)], \quad (1)$$

where  $m$  are the masses in the source frame,  $P_s[m(z_m)]$  is the source frame mass distribution at redshift  $z_m$  and  $W_{t_d}[m(z_m)]$  is the window function that takes into account the delay time of the mergers. The masses in the detector frame, or redshifted masses, are given by

$$m^{\text{det}} = (1+z)m, \quad (2)$$

The window function is calculated using:

$$W_{t_d}[m(z_m)] = N \int_{z_m}^{\infty} P_t(t_d | t_d^{\text{min}}, t_d^{\text{max}}, d) \frac{dt}{dz_f} W[m(z_f)] dz_f, \quad (3)$$

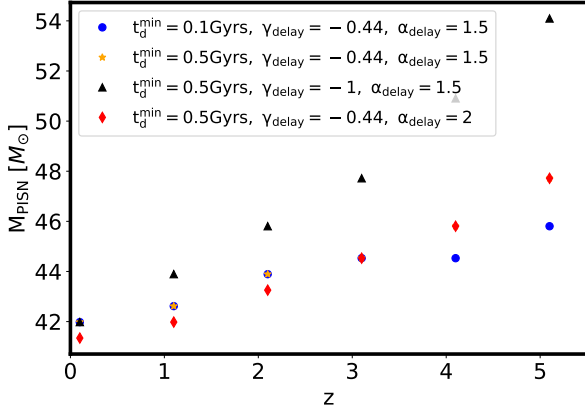


**Figure 1.** The position of the  $M_{\text{PISN}}$  as a function of redshift varying different parameters. The plot was created with fixed  $d = -1$ ,  $H_0 = 70$  km/s/Mpc and  $\Omega_m = 0.3$ . Varying  $d$  does not affect the position of  $M_{\text{PISN}}$ .

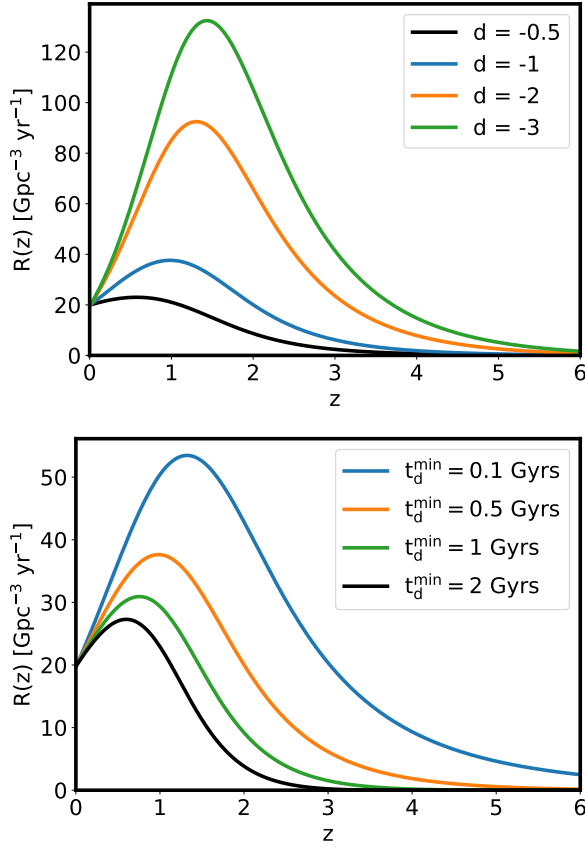


**Figure 2.** The merger rate function  $R(z)$  for various values of the parameters  $d$ ,  $t_d^{\text{min}}$  and for fiducial flat Cold Dark Matter cosmology with a constant energy density for dark energy and  $H_0 = 70$  km/s/Mpc and  $\Omega_m = 0.3$ . Top: Fixing  $t_d^{\text{min}} = 0.5$  Gyrs and varying  $d$ . Bottom: Fixing  $d = -1$  and varying  $t_d^{\text{min}}$ .

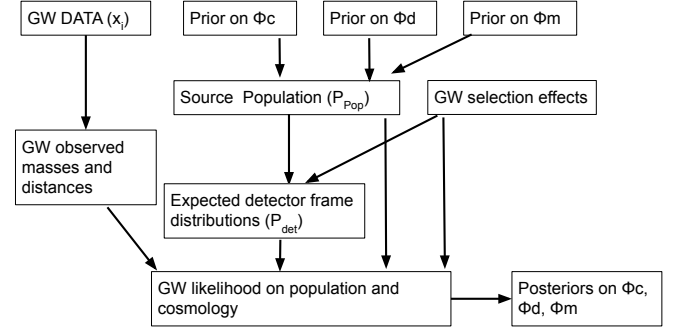


**Figure 3.** A flow chart diagram visualizing the framework of the method that we use to calculate the posteriors.

where  $N$  is a normalization factor,  $P_t$  is the delay time distribution,  $W[m(z)]$  is a window function that gradually drops to 0 after  $M_{\text{PISN}}$  depending on the formation scenario and  $z_f$  is the redshift of the formation of a black hole. The delay time distribution is taken to be a simple power-law function of the delay time  $t_d$ :

$$P_t(t_d | t_d^{\text{min}}, t_d^{\text{max}}, d) \propto \begin{cases} (t_d)^d & , \text{ for } t_d^{\text{min}} < t_d < t_d^{\text{max}} \\ 0 & , \text{ otherwise} \end{cases}, \quad (4)$$

and the delay time is given by  $t_d = t_m - t_f$ , with the notation  $t_m = t(z_m)$ ,  $t_f = t(z_f)$  to be the time of merger and time of formation respectively.

Assuming the dependence of the PISN mass scale on metallicity  $M_{\text{PISN}}(Z)$  studied by [Spera & Mapelli \(2017\)](#); [Farmer et al. \(2019\)](#); [Renzo et al. \(2020\)](#) can be reliably scaled using a parameter  $\alpha_{\text{delay}}$  ([Mukherjee 2021](#)), we can then model it with metallicity as:

$$M_{\text{PISN}}(Z) = M_{\text{PISN}}(Z_*) - \alpha_{\text{delay}} \log(Z/Z_*), \quad (5)$$

and for a power-law redshift evolution of the stellar metallicity (as supported by the current observations ([Mannucci et al. 2010](#); [Sommariva et al. 2012](#); [Krumholz & Dekel 2012](#); [Dayal et al. 2013](#); [Madau & Dickinson 2014](#))), we can write the redshift dependence of metallicity as  $\log Z(z) = \gamma_{\text{delay}} z + \zeta$ . Consequently, the previous equation can be written as:

$$M_{\text{PISN}}(z) = M_{\text{PISN}}(Z_*) - \alpha_{\text{delay}} [\gamma_{\text{delay}} z + \zeta - \log(Z_*)], \quad (6)$$

where  $\zeta$  is taken to be a constant to match the low redshift measurement of the stellar metallicity  $Z(z=0) \approx 10^{-2}$ . We show the value of the PISN mass scale as a function of redshift for different values of minimum delay time  $t_d^{\text{min}}$ , metallicity evolution with redshift  $\gamma_{\text{delay}}$ , and evolution of PISN mass scale with redshift  $\alpha_{\text{delay}}$  in Fig. 1. The above expression is written in terms of the global evolution of stellar metallicity with redshift. However, at any particular redshift, there is going to be additional variation in the stellar metallicity depending on the property of the host galaxy. So, we would expect variation in the parameter  $\gamma_{\text{delay}}$  on the property of the host galaxy. However, currently, due to the poor sky location error of the GW sources, we cannot identify the host galaxy and hence cannot model the parameter  $\gamma_{\text{delay}}$  as a function of the galaxy. As a result, there can be an additional variation in the  $\gamma_{\text{delay}}$  that cannot be well modeled currently. Similarly, the parameter  $\alpha_{\text{delay}}$  controls the dependence of the PISN

mass scale on the metallicity (Farmer et al. 2019). Hence we treat both these parameters as nuisance parameters in this analysis.

The merger rate density of the BBHs can be related to the Madau-Dickinson SFR denoted by  $R_{SFR}(z)$  (Madau & Dickinson 2014) by the relation

$$R(z_m) = R_0 \frac{\int_{z_m}^{\infty} P_t(t_d | t_d^{\min}, t_d^{\max}, d) R_{SFR}(z_f) \frac{dt}{dz_f} dz_f}{\int_0^{\infty} P_t(t_d | t_d^{\min}, t_d^{\max}, d) R_{SFR}(z_f) \frac{dt}{dz_f} dz_f}, \quad (7)$$

here,  $R_0 \equiv R(z=0)$  is defined as the merger rate at  $z=0$ <sup>1</sup>. We show the BBH merger rate for a few values of the variables  $d$ ,  $t_d^{\min}$  and for a fiducial flat Lambda Cold Dark Matter (LCDM) cosmology model with  $H_0 = 70 \text{ km/s/Mpc}$  and  $\Omega_m = 0.3$  in Fig. 2 with  $R_0 = 20 \text{ Gpc}^{-3} \text{ yr}^{-1}$ . The plot indicates that with the decrease in the value of power-law index  $d$  and minimum delay time  $t_d^{\min}$ , the peak in the BBH merger shifts towards a higher redshift with a steeper slope at low redshift. Current observations from LVK can measure BBHs at redshifts ( $z < 1$ ) (for a fiducial model of cosmology). As a result, we can primarily constrain the minimum delay time  $t_d^{\min}$  and the power-law index  $d$  from the low redshift slope.

The above discussion shows that the delay time distribution  $P_t(t_d | t_d^{\min}, t_d^{\max}, d)$  plays a role in both the mass distribution of the BHs and also in their merger rates. As a result, to infer the BBH formation channel and the delay time distribution, it will be necessary to use both merger rate and mass distribution to infer the delay time distribution of BBHs. Moreover, to estimate the redshift of the BHs from their mass distribution, one needs to account for the redshift dependence of the BBH mass distribution. As a result, we need to conjointly infer the cosmological parameters along with the delay time distribution of BHs, and the black hole mass distribution, to correctly marginalize the degenerate parameters.

### 3 BAYESIAN FRAMEWORK TO INFER COSMOLOGY FROM GW POPULATION

We construct a Bayesian model following the method described in (Mastrogiovanni et al. 2021b; Virgo & Kagra 2021) to conjointly infer the redshift dependence of the mass distribution and merger rate along with the cosmological parameters. In Fig. 3 we show a schematic diagram explaining the formalism. We discuss below each part that goes into the analysis. For our model, the set of hyper-parameters  $\Phi$  that are common to the entire population are the cosmological, the source frame mass distribution and delay time parameters  $\Phi = \{\Phi_m, \Phi_{\text{cosmo}}, \Phi_{\text{delay}}, \Phi_{\text{nuis}}\}$ . As a cosmological model, we consider a flat LCDM (Aghanim et al. 2018). Given a set of  $N$  GW detections associated with the data  $\{x\} = (x_1, \dots, x_N)$ , the posterior on  $\Phi$  can be expressed as (Mastrogiovanni et al. 2021b; Virgo & Kagra 2021; Vitale et al. 2021; Thrane &

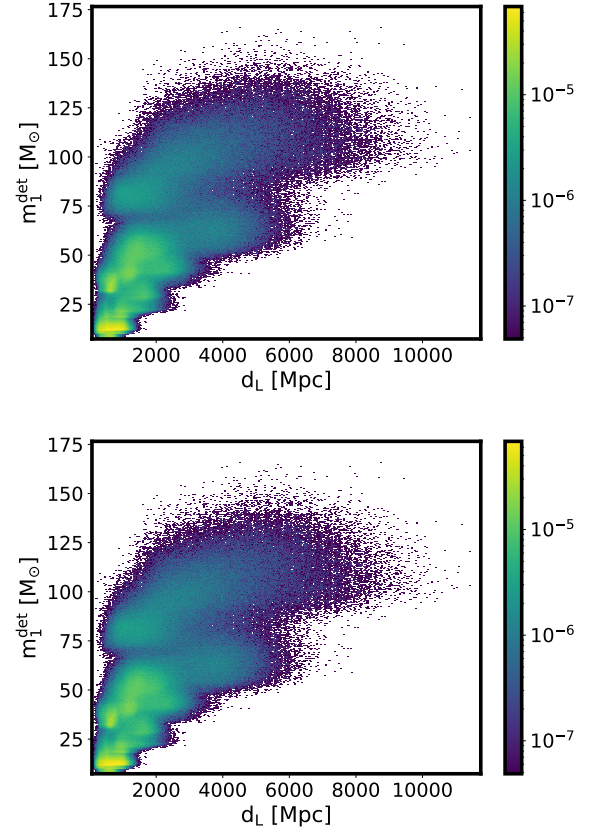


**Figure 4.** Two dimensional plots of the detector frame masses and distance posterior samples for all GW events with  $SNR \geq 12$ . In the colorbar there is the probability in logarithmic scale. Top plot: Samples of the heavy component  $m_1^{\text{det}}$ . Bottom plot: Samples of the light component  $m_2^{\text{det}}$ .

(Talbot 2019; Mandel et al. 2019)

$$p(\Phi, \{x\}, N) = \Pi(\Phi) e^{-N_{\text{exp}}(\Phi)} N_{\text{exp}}(\Phi)^{N_{\text{obs}}} \times \prod_{i=1}^N \frac{\int p(x_i | \Phi, \theta) p_{\text{pop}}(\theta | \Phi) d\theta}{\int p_{\text{det}}(\Phi, \theta) p_{\text{pop}}(\theta | \Phi) d\theta}, \quad (8)$$

where  $\Pi(\Phi)$  is the prior on the parameters,  $\theta$  is the set of intrinsic parameters, which are unique for each event,  $p(x_i | \Phi, \theta)$  is the likelihood,  $p_{\text{det}}(\theta, \Phi)$  is the probability of detection and  $p_{\text{pop}}(\theta | \Phi)$  is the population modelled prior. Finally,  $N_{\text{exp}}(\Phi)$  is the expected number of detections in a given observing time and  $N_{\text{obs}}$  the number of events considered in the analysis.

The term  $p_{\text{pop}}(\theta | \Phi)$  is equal to:

$$p_{\text{pop}}(\theta | \Phi) = CP[m(z)] \frac{R(z)}{1+z} \frac{dV_c}{dz}, \quad (9)$$

where  $C$  is a normalization constant and  $dV_c/dz$  is the comoving volume element. This term captures the effects of delay time between formation and merger.

The denominator of Eq. 8 normalizes the numerator and takes into account the selections effects (Mastrogiovanni et al. 2021b; Virgo & Kagra 2021). It is written as an integral over all detectors' data that pass certain detection criteria for given known noise properties of the detectors. The term  $p_{\text{det}}(\theta, \Phi)$  is the probability of detecting the source with parameters  $\theta$  and assuming hyper-parameters  $\Phi$ .

<sup>1</sup> It is not defined as the normalization constant to match total number of sources, but rather the merger rate at  $z=0$ .

## Delay time + Merger rate parameters

Parameter	Description	Prior
$d$	Spectral index for the power-law of the delay time distribution.	$\mathcal{U}(-4,0)$
$t_d^{\min}$	Minimum time for the power-law of the delay time distribution in Gyrs.	$\mathcal{U}(0.01,13)$
$R_0$	Value of the merger rate at $z = 0$ in $\text{Gpc}^{-3} \text{yr}^{-1}$ .	$\mathcal{U}(0,1000)$

## Mass distribution parameters

Parameter	Description	Prior
$\alpha$	Spectral index for the power-law of the primary mass distribution.	$\mathcal{U}(-4,12)$
$\beta$	Spectral index for the power-law of the mass ratio distribution.	$\mathcal{U}(-4,12)$
$M_{\min}$	Minimum mass of the power-law component of the primary mass distribution in $M_{\odot}$ .	$\mathcal{U}(2,10)$
$M_{\max}$	Maximum mass of the power-law component of the primary mass distribution in $M_{\odot}$ .	$\mathcal{U}(50,200)$
$\lambda_g$	Fraction of the model in the Gaussian component.	$\mathcal{U}(0,1)$
$\mu_g$	Mean of the Gaussian component in the primary mass distribution in $M_{\odot}$ .	$\mathcal{U}(20,60)$
$\sigma_g$	Width of the Gaussian component in the primary mass distribution in $M_{\odot}$ .	$\mathcal{U}(0.4,10)$
$\delta_m$	Range of mass tapering at the lower end of the mass distribution in $M_{\odot}$ .	$\mathcal{U}(0,10)$

## Cosmological parameters (Flat LCDM model)

Parameter	Description	Prior
$H_0$	The Hubble constant parameter in $\text{km/s/Mpc}$ .	$\mathcal{U}(20,150)$
$\Omega_m$	Present-day matter density of the Universe.	0.315 (fixed)

## Nuisance parameters

Parameter	Description	Prior
$\alpha_{\text{delay}}$	The parameter that captures a weak logarithmic dependence of $M_{\text{PISN}}$ on the metallicity.	$\mathcal{U}(0,3)$
$\gamma_{\text{delay}}$	The parameter that captures the redshift dependence of the metallicity.	$\mathcal{U}(-3,0)$

**Table 1.** Summary of the hyper parameters and the priors used. The distribution  $\mathcal{U}(\min, \max)$  is just a uniform distribution between min and max for each parameter.

The source frame mass distribution is taken to be:

$$P_s(m_1, m_2 | \Phi_m) = p(m_1 | \Phi_m) p(m_2 | m_1, \Phi_m) S_1 S_2, \quad (10)$$

where  $p(m_1 | \Phi_m)$  is the distribution of  $m_1$  and  $p(m_2 | m_1, \Phi_m)$  is the distribution of  $m_2$ , conditioned on the constraint  $m_1 \geq m_2$ , and  $S_{(1,2)} = S(m_{(1,2)} | \delta_m, M_{\min})$  are sigmoid-like window functions to smooth the lower end of the distributions (see appendix A of (Virgo & Kagra 2021)).

The distribution of  $m_1$  in the source frame is considered to be given by a power-law distribution superpositioned with the distribution of a Gaussian peak:

$$p(m_1 | \Phi_{m_1}) = (1 - \lambda_g) P(m_1 | M_{\min}, M_{\max}, -\alpha) + \lambda_g G(m_1 | \mu_g, \sigma_g), \quad (11)$$

where  $\Phi_{m_1} = \{M_{\min}, M_{\max}, \alpha, \lambda_g, \mu_g, \sigma_g\}$ ,  $G(m_1 | \mu_g, \sigma_g)$  is a Gaussian distribution with  $\mu = \mu_g$  and  $\sigma = \sigma_g$  and  $P(m_1 | M_{\min}, M_{\max}, -\alpha)$  is a power-law distribution with slope  $-\alpha$  between  $M_{\min}$  and  $M_{\max}$ .

The distribution of  $m_2$  in the source frame is considered to be given by a power-law distribution with maximum value  $m_1$ :

$$p(m_2 | \Phi_{m_2}) = P(m_2 | M_{\min}, m_1, \beta). \quad (12)$$

The summary of the priors used for the parameters that we consider in our model can be found in Tab. 1. We also perform population fits of the distribution of BBHs using the

three redshift-independent source-frame mass phenomenological models and merger rate models used in Virgo & Kagra (2021). The priors that we use for this set of runs are the same as the ones used in Virgo & Kagra (2021) with the difference in the cosmological parameters. In the two set of runs that we perform, the dark energy equation of state parameter  $w_0$  and  $\Omega_m$  are fixed to  $-1$  and  $0.308$ , while for the first set of runs the  $H_0$  is fixed to  $67.7 \text{ km s}^{-1} \text{ Mpc}^{-1}$  and for the second we use a uniform prior in  $[20, 150] \text{ km s}^{-1} \text{ Mpc}^{-1}$ .

## 4 RESULTS FROM GWTC-3

We analyzed all the BBH events from GWTC-3 (Abbott et al. 2021c; Buikema et al. 2020) with the matched filtering Signal-to-Noise Ratio (SNR) in at least one of the detection pipelines higher than 12 (results with the  $\text{SNR} \geq 11$  are presented in appendix A). For all the events, we also require a False Alarm Rate  $< 0.25 \text{ yr}^{-1}$ . For the results in this section, we do not consider GW190521, as it is expected to belong to a second generation BHs (results with the inclusion of this event can be found in B). A previous study has also found stronger evidence in favor of GW190521 being a second-generation BBH source and other BBHs sources did not show up very strong support in favor of the second-generation sources Kimball et al. (2021). The mass and luminosity distance distributions

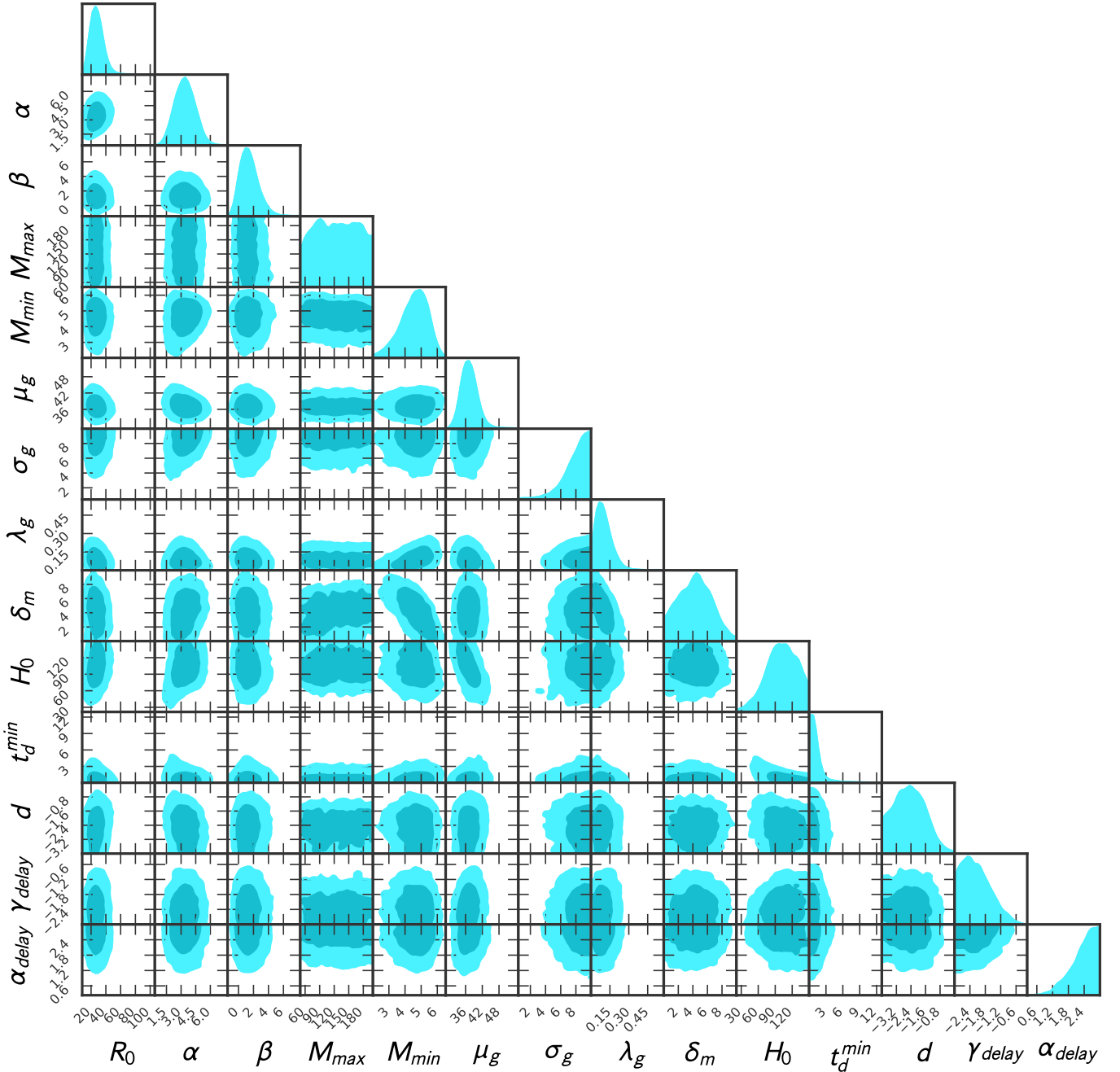


**Figure 5.** Posterior distributions for all the hyper parameters. Here we have fixed all cosmological parameters besides  $H_0$  at Planck-2018 cosmology. We have used all GW events with  $SNR \geq 12$ . This plot corresponds to case 1 mentioned in the results section.

of the GWTC-3 catalog for sources with  $SNR \geq 12$  can be seen in Fig. 4. To correct selection biases, we take into account detector sensitivity and detector duty cycles. We consider three sets of population priors in this analysis, *Case-1*: We fix the cosmological parameters besides the Hubble constant and consider only priors on the population parameters describing the BBHs distribution (other cosmological parameters are kept fixed at Planck-2018 cosmology (Aghanim et al. 2018)), *Case-2*: as Case-1 but we keep the value of the delay time power-law index fixed and equal to  $d = -1$ , which is usually assumed as a fiducial scenario for flat in the log-

space distribution of the separation between the binaries, and *Case-3*: we keep fixed the values of the cosmological parameters to Planck-2018 (Aghanim et al. 2018) and estimate the parameters which are related to the GW source population. The analysis for Case-2 (with a fixed value of  $d = -1$ ) is motivated to find the constraints on the parameter space for the fiducial scenario of the delay time distribution, which resembles closely the previous analysis (Abbott et al. 2021b). We consider the third case to infer the value of the GW source parameters assuming a fixed cosmology. Though the choice of cosmological parameters can influence the inferred values of

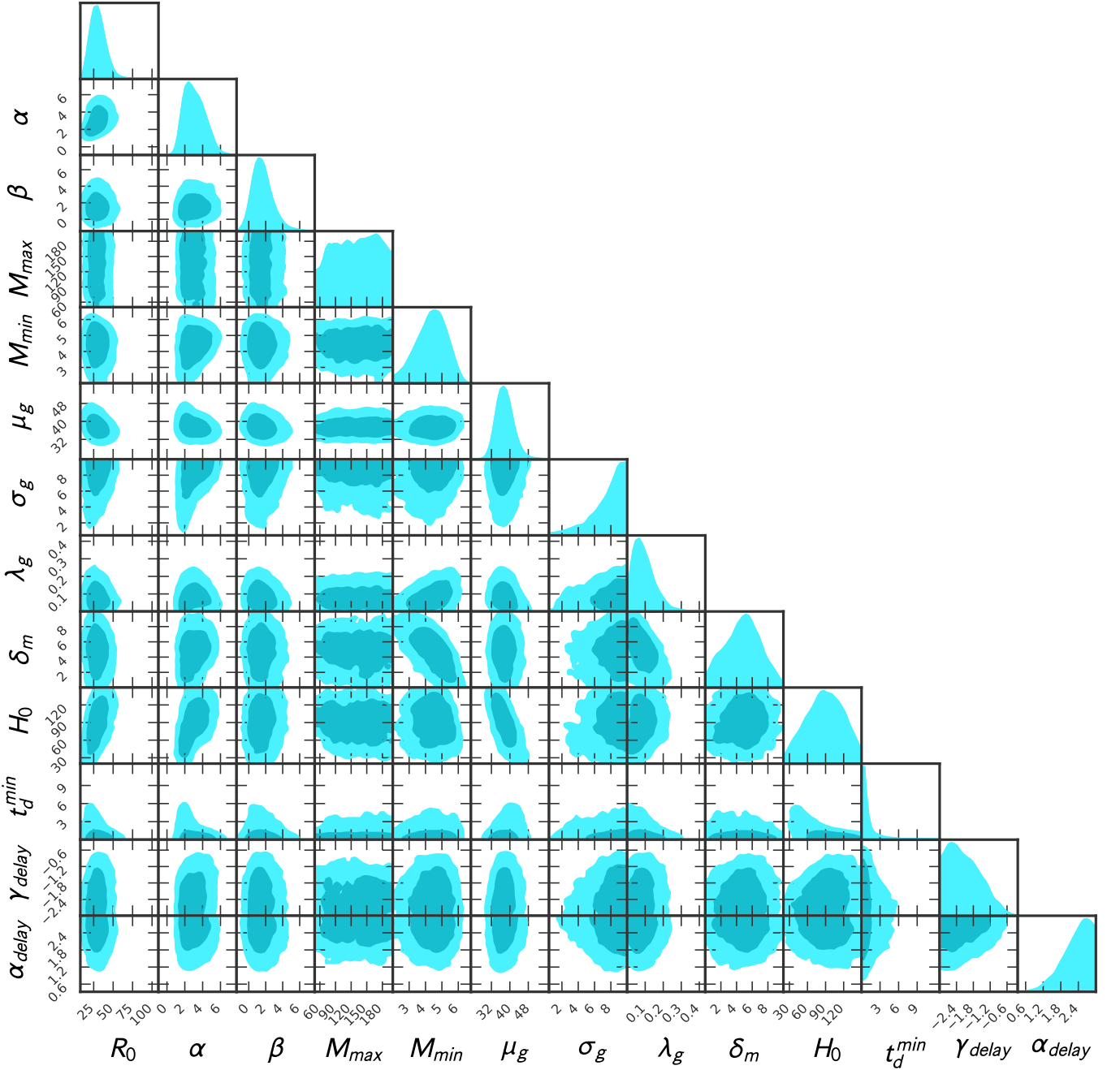


**Figure 6.** Posterior distributions for all the hyper parameters. Here we have fixed all cosmological parameters besides  $H_0$  at Planck-2018 cosmology. We have fixed the power-law index of the delay time to  $d = -1$ . We have used all GW events with  $SNR \geq 12$ . This plot corresponds to case 2 mentioned in the results section.

the GW source parameters, given the current precision of the cosmological parameters from Planck-2018, the expected statistical error in the inferred GW source parameters is much larger than the systematic error due to different choices in the value of  $H_0 = 66.9$  km/s/Mpc (Aghanim et al. 2018) or  $H_0 = 73$  km/s/Mpc (Riess et al. 2021). The priors of the runs for each of the parameters can be found in Table 1. We have summarised the estimated values of the parameters for different cases in Table 2. All the quoted values of the error bars are 68% confidence intervals unless mentioned otherwise.

*Case-1 (GW source population +  $H_0$ ):* For this scenario, the joint constraints on the 13 GW source population parameters and one cosmological parameter  $H_0$  is shown in Fig. 5. The joint estimation can be broadly classified into the parameters related to the delay time + merger rate, mass distribution, and cosmology. Among the delay time + merger rate parameters, we find that data supports a scenario of a steep increase in the redshift evolution of the merger rate ( $d < -1$ ), with BBHs merger rate density at  $z = 0$   $R_0 = 26.87^{+8.42}_{-7.04}$   $\text{Gpc}^{-3} \text{ yr}^{-1}$ . Due to modeling the GW merger rate with

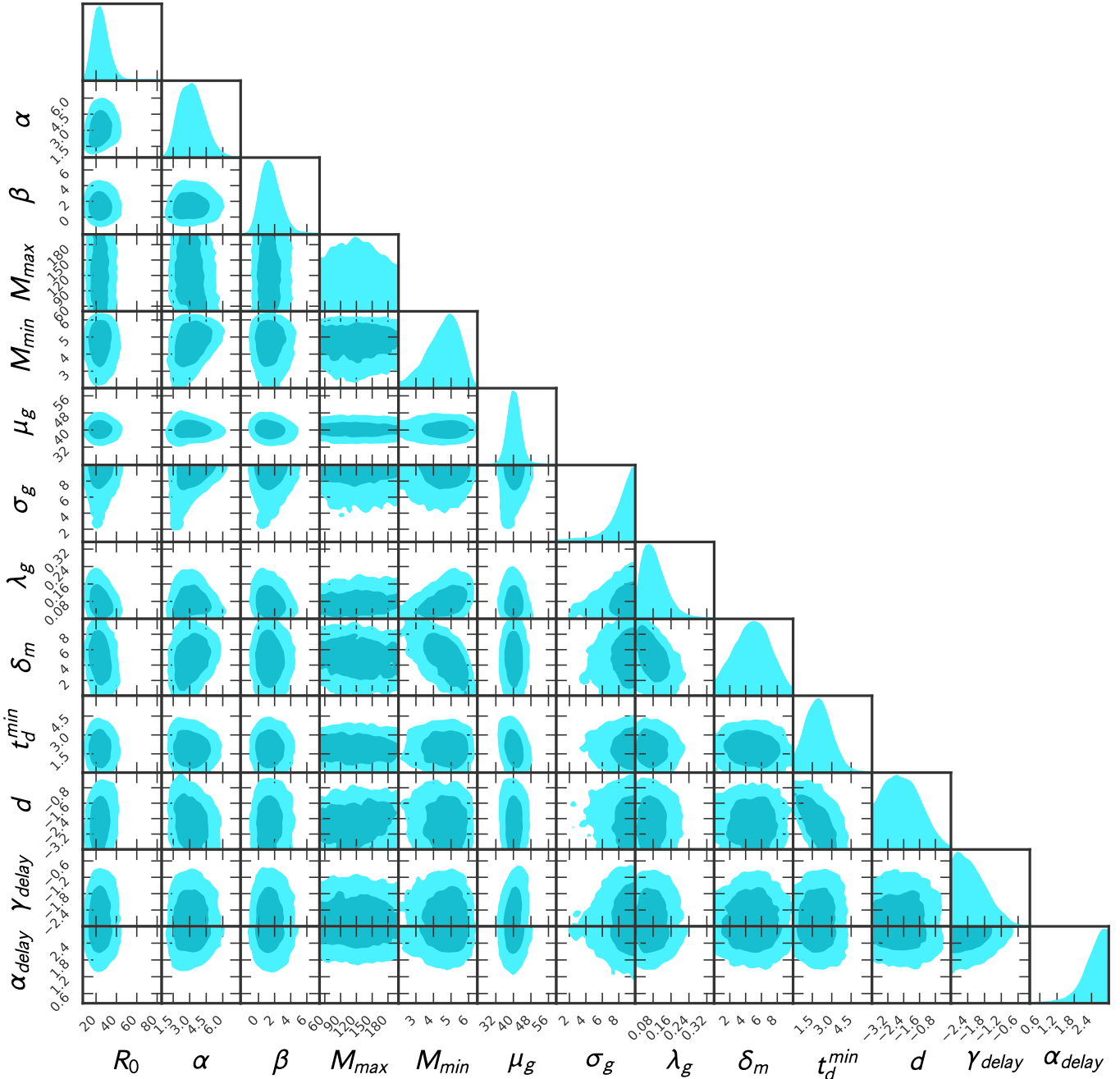


**Figure 7.** Posterior distributions for all the hyper parameters. Here we have fixed all cosmological parameters at Planck-2018 cosmology. We have used all GW events with  $SNR \geq 12$ . This plot corresponds to case 3 mentioned in the results section.

the Madau-Dickinson star formation rate, the merger rate at high redshift is significantly constrained. These constraints are solely driven by the constraints from delay time distribution. However, if there is a different population of BBHs that do not contribute to low redshifts according to the Madau-Dickinson SFR, but contributes to the high redshift such as the Pop-III star, that cannot be constrained from this analysis. The expected number of events after including the detector noise and duty cycle agrees well with the total number of events with  $SNR \geq 12$  considered in this analysis.

Using this model, we impose stringent constraints on the

minimum delay time distribution  $t_d^{\min} < 1.81^2$  Gyrs. The value of the minimum delay time distribution shows a non-zero value (at around  $1-\sigma$  away from zero). This is driven by the joint estimation of the merger rate and mass distribution of the BBHs. However, due to the fewer GW sources, it is difficult to draw a clear conclusion. The value of the power-law index of the delay time distribution  $d < -1.62$  and does not strongly support the value of  $d = -1$  as expected from

<sup>2</sup> Upper limits are based on the upper 68% CL

Parameters	Pop+H <sub>0</sub>	Pop(d=-1)+H <sub>0</sub>	Pop	Pop+H <sub>0</sub> inc. GW190521	Pop+H <sub>0</sub> with SNR ≥ 11
R <sub>0</sub> [Gpc <sup>-3</sup> yr <sup>-1</sup> ]	26.87 <sup>+8.42</sup> <sub>-7.04</sub>	29.55 <sup>+9.85</sup> <sub>-7.98</sub>	24.06 <sup>+7.34</sup> <sub>-5.85</sub>	23.03 <sup>+7.28</sup> <sub>-5.94</sub>	24.6 <sup>+7.49</sup> <sub>-5.92</sub>
α	3.39 <sup>+1.01</sup> <sub>-1.0</sub>	2.97 <sup>+1.3</sup> <sub>-0.99</sub>	3.14 <sup>+1.12</sup> <sub>-1.02</sub>	1.99 <sup>+0.74</sup> <sub>-0.48</sub>	3.66 <sup>+1.02</sup> <sub>-1.05</sub>
β	1.31 <sup>+1.28</sup> <sub>-1.01</sub>	1.48 <sup>+1.24</sup> <sub>-0.95</sub>	1.4 <sup>+1.26</sup> <sub>-1.0</sub>	1.28 <sup>+1.09</sup> <sub>-0.93</sub>	1.21 <sup>+1.19</sup> <sub>-1.01</sub>
M <sub>max</sub> [M <sub>⊙</sub> ]	125.73 <sup>+48.4</sup> <sub>-47.65</sub>	130.67 <sup>+44.67</sup> <sub>-49.95</sub>	122.01 <sup>+48.58</sup> <sub>-46.01</sub>	138.97 <sup>+39.81</sup> <sub>-39.82</sub>	126.28 <sup>+47.73</sup> <sub>-47.89</sub>
M <sub>min</sub> [M <sub>⊙</sub> ]	4.63 <sup>+0.74</sup> <sub>-0.92</sub>	4.42 <sup>+0.83</sup> <sub>-1.0</sub>	4.67 <sup>+0.77</sup> <sub>-1.04</sub>	4.28 <sup>+1.01</sup> <sub>-1.1</sub>	4.67 <sup>+0.67</sup> <sub>-0.82</sub>
μ <sub>g</sub> [M <sub>⊙</sub> ]	37.12 <sup>+2.88</sup> <sub>-2.42</sub>	37.59 <sup>+3.64</sup> <sub>-3.11</sub>	40.26 <sup>+2.35</sup> <sub>-2.32</sub>	38.12 <sup>+3.52</sup> <sub>-2.98</sub>	37.25 <sup>+2.96</sup> <sub>-2.49</sub>
σ <sub>g</sub> [M <sub>⊙</sub> ]	8.34 <sup>+1.16</sup> <sub>-1.88</sub>	8.16 <sup>+1.28</sup> <sub>-2.5</sub>	8.72 <sup>+0.93</sup> <sub>-1.89</sub>	7.4 <sup>+1.8</sup> <sub>-3.32</sub>	8.43 <sup>+1.11</sup> <sub>-1.79</sub>
λ <sub>g</sub>	0.09 <sup>+0.07</sup> <sub>-0.05</sub>	0.08 <sup>+0.07</sup> <sub>-0.05</sub>	0.08 <sup>+0.06</sup> <sub>-0.04</sub>	0.05 <sup>+0.05</sup> <sub>-0.03</sub>	0.08 <sup>+0.06</sup> <sub>-0.04</sub>
δ <sub>m</sub> [M <sub>⊙</sub> ]	4.34 <sup>+2.22</sup> <sub>-2.45</sub>	4.86 <sup>+2.15</sup> <sub>-2.49</sub>	4.9 <sup>+2.2</sup> <sub>-2.4</sub>	4.08 <sup>+2.55</sup> <sub>-2.42</sub>	4.96 <sup>+1.89</sup> <sub>-1.98</sub>
H <sub>0</sub> [km s <sup>-1</sup> Mpc <sup>-1</sup> ]	102.55 <sup>+27.22</sup> <sub>-27.61</sub>	89.4 <sup>+30.87</sup> <sub>-32.32</sub>	—	82.42 <sup>+36.85</sup> <sub>-32.44</sub>	105.24 <sup>+26.94</sup> <sub>-30.1</sub>
t <sub>d</sub> <sup>min</sup> [Gyrs]	0.85 <sup>+0.96</sup> <sub>-0.5</sub>	0.46 <sup>+1.43</sup> <sub>-0.35</sub>	1.95 <sup>+0.97</sup> <sub>-0.93</sub>	1.39 <sup>+2.31</sup> <sub>-0.89</sub>	0.95 <sup>+0.99</sup> <sub>-0.57</sub>
d	-2.49 <sup>+0.87</sup> <sub>-0.89</sub>	—	-2.53 <sup>+0.98</sup> <sub>-0.89</sub>	-2.32 <sup>+1.02</sup> <sub>-0.96</sub>	-2.32 <sup>+0.93</sup> <sub>-0.97</sub>
γ <sub>delay</sub>	-2.22 <sup>+0.32</sup> <sub>-0.65</sub>	-2.19 <sup>+0.69</sup> <sub>-0.53</sub>	-2.33 <sup>+0.62</sup> <sub>-0.45</sub>	-2.52 <sup>+0.52</sup> <sub>-0.23</sub>	-2.14 <sup>+0.71</sup> <sub>-0.57</sub>
α <sub>delay</sub>	2.47 <sup>+0.37</sup> <sub>-0.59</sub>	2.42 <sup>+0.39</sup> <sub>-0.57</sub>	2.58 <sup>+0.29</sup> <sub>-0.45</sub>	2.61 <sup>+0.27</sup> <sub>-0.42</sub>	2.39 <sup>+0.41</sup> <sub>-0.58</sub>
N <sub>exp</sub>	35 <sup>+6</sup> <sub>-5</sub>	34 <sup>+6</sup> <sub>-5</sub>	35 <sup>+6</sup> <sub>-5</sub>	36 <sup>+6</sup> <sub>-5</sub>	41 <sup>+6</sup> <sub>-5</sub>
N <sub>events</sub>	34	34	34	35	41

**Table 2.** The median estimations of all parameters along with the 68% credible levels can be seen here. The  $N_{\text{exp}}$  and  $N_{\text{events}}$  rows indicate the expected number of events in each case using the median value and are derived from the estimated parameters and the number of events detected above an SNR threshold from GWTC-3 respectively.

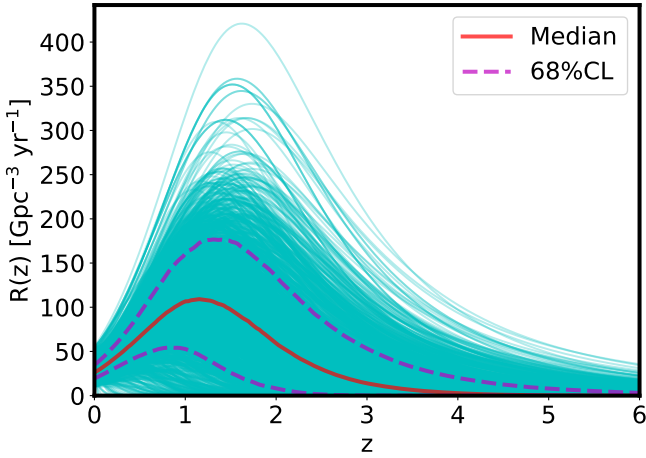


**Figure 8.** The merger rate evolution as a function of redshift for different posterior samples (cyan curves) of the various parameters. In the same plot the median (red solid curve) and the 68% credible levels (purple dashed curves) can also be seen. The cases with a fixed value are shown with the fixed mean value and zero uncertainty.

a simple scenario of flat in the log-space distribution of object separation of the binaries. This measurement shows a much steep distribution of the delay time and hints towards scenario formation channels having less probability of large delay time. Though the current measurement of the delay time distribution only shows a weak detection, in the future with the availability of more data and a better understanding of the delay time distribution and formation channel can be explored. We have also discussed later our results from the case with a fixed value  $d = -1$  and a case with a value of  $H_0 = 67.4 \text{ km s}^{-1} \text{ Mpc}^{-1}$  in agreement with the value from the Planck collaboration (Aghanim et al. 2018). The BBHs with heavier component masses in the data are fitted with BHs appearing from a higher redshift with higher PISN masses

and a non-zero value of the delay time distribution. For values with small minimum delay time distribution, the black hole would have arisen from local redshift, and could not fit the data of mass and luminosity distance distribution with the low redshift stellar metallicity.

This value of the parameter  $\gamma_{\text{delay}} < -1.57$  indicates an upper bound and posterior is consistent with the estimation of the redshift evolution of the stellar metallicity in the Universe made from electromagnetic observations (Mannucci et al. 2010; Sommariva et al. 2012; Krumholz & Dekel 2012; Dayal et al. 2013; Madau & Dickinson 2014) and also proposed from simulations (Genel 2016; Torrey et al. 2019). However, depending on the metallicity of the host galaxy, this parameter cannot be easily related to the mean metallicity evolution and can show additional variation (Artale et al. 2019, 2020).

The parameters related to the mass distribution are also constrained well using a model that allows for the redshift-dependent mass distribution. We have obtained a value of the power-law index of the mass distribution  $\alpha = 3.39^{+1.01}_{-1.0}$  and  $\beta = 1.31^{+1.28}_{-1.01}$ . We also find the presence of a Gaussian bump in the mass distribution (in agreement with the LVK estimation (Abbott et al. 2021b)) with a relative height  $\lambda_g = 0.09^{+0.07}_{-0.05} M_{\odot}$ , a variance of  $\sigma_g > 6.46 M_{\odot}$  and the position of the peak  $\mu_g = 37.12^{+2.88}_{-2.42} M_{\odot}$ . The position of the peak agrees with the theoretically predicted position of the PISN mass scale between 45-60  $M_{\odot}$  (Farmer et al. 2019; Renzo et al. 2020) within 1- $\sigma$ . The posterior distribution of the  $\mu_g$  parameter is shown separately in Fig. 9 (bottom, blue curve). This result differs from a lower value of the  $\mu_g$  parameter obtained previously (Abbott et al. 2021b; Virgo & Kagra 2021), and the peak of the distribution of these previous estimates are less in the agreement with the theoretical predictions of the PISN mass scale. As shown in Fig. 10, the redshift evolution of the PISN mass scale does not show any statistically significant variation over the redshift range  $z \in [0, 1]$ . Previously redshift dependence of different phenomenological models of BBH mass distribution was ex-

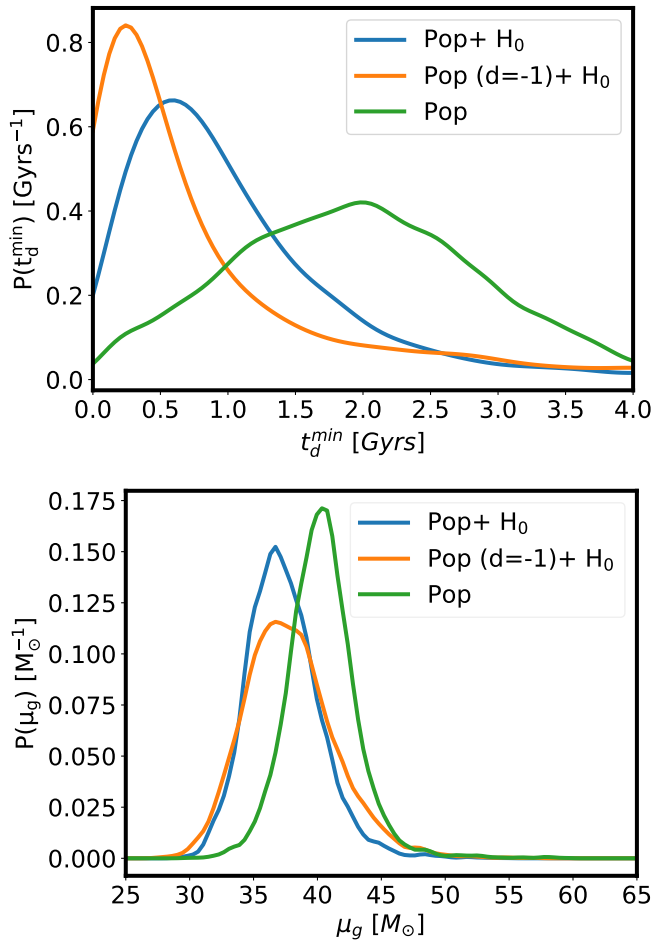


**Figure 9.** Posteriors on  $t_d^{\min}$  (top) and  $\mu_g$  (bottom) for the three cases that we considered. Case 1: Keeping all the cosmological parameters besides  $H_0$  fixed to Planck 2018 values and estimate  $H_0$ +population parameters (labeled as Pop+ $H_0$ ). Case 2: Keep all the cosmological parameters besides  $H_0$  fixed to Planck 2018 values but also consider a fiducial fixed delay time power-law index  $d = -1$  and estimate the rest of the population parameters+ $H_0$  (labeled as Pop( $d=-1$ )+ $H_0$ ). Case 3: Fix all cosmological parameters to Planck 2018 values and estimate all of the population parameters (labeled as Pop).

explored from GWTC-2 (Fishbach et al. 2021). They found strong evidence for the redshift evolution of the mass model when considering a truncated power law with a sharp cut-off at high masses. However, the data were consistent with both an evolving and a non-evolving mass distribution when they considered a broken power-law model as a mass model. Those findings are in agreement with our results since the redshift dependence that we find using the current data is weak.

We find other parameters do not show up significant deviation from previous results (Abbott et al. 2021b; Virgo & Kagra 2021). However, differently from (Abbott et al. 2021b; Virgo & Kagra 2021), in our model, the value of  $m_{\max}$  can not be constrained. This is because high mass GW events are suppressed after  $M_{\text{PISN}}$ . In Fig. 11, we show the differential in the mass of the BBHs merger rate distribution as a function of redshift. The figure is computed using the median of the population parameters reported in Fig. 5 along with the

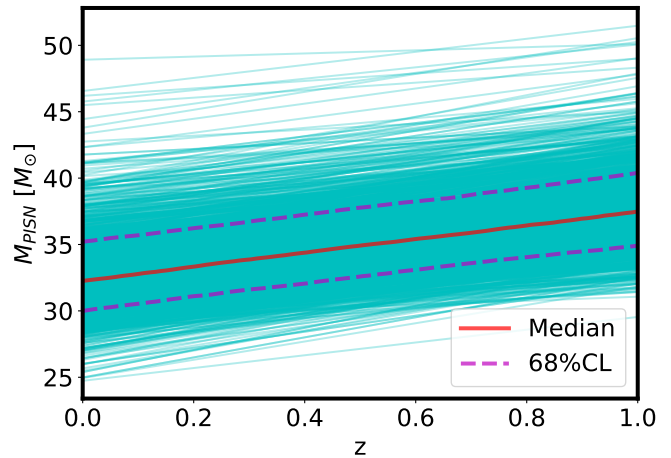


**Figure 10.** The  $M_{\text{PISN}}$  position as a function of redshift for different posterior samples (cyan curves). In the same plot the median (red solid curve) and the 68% credible levels (purple dashed curves) can also be seen.

68% C.L. showed by shaded regions. As we can see from the figure, the excess of BBHs associated with the PISN evolves from lower and narrower values at low redshifts to higher and shallower values at higher redshifts. Most importantly, this model highly suppresses high mass GW events, that happen to be observed after the PISN limit. As a result, this model struggles in fitting the high mass GW ( $> 50M_\odot$ ) events that are currently observed. As the model explored in this analysis, is only applicable to first-generation BBH mergers and fails to capture any second-generation (or non-astrophysical BBHs of higher masses), it shows a poor fit to the data with a Bayes factor around  $10^3$  in comparison to the phenomenological POWER-LAW+PEAK redshift-independent mass model employed in (Virgo & Kagra 2021). With respect to the Truncated power-law redshift-independent mass model, which also suppresses higher mass BBHs, we find that our model is  $\sim 10$  times less preferred due to the increased number of nuisance parameters. This implies that a theoretical model which can capture both first and second-generation BBHs along with the redshift dependence of the mass distribution will be interesting to explore in the future. In follow-up work, we will show the parameter estimation of such a model from GWTC-3.

Finally, a weak measurement of the Hubble constant  $H_0 = 102.55^{+27.22}_{-27.61}$  km/s/Mpc is made which is in the agreement with the values from Planck-2018 (Aghanim et al. 2018), SH0ES (Riess et al. 2021) due to a large uncertainty in the current measurements. It is important to note the correlation between the Hubble constant and the delay time distribution parameters in Fig. 5. This indicates that not being able to correctly infer the PISN mass scale can lead to an incorrect inference of the cosmological parameters (Mukherjee 2021).

We also compare the results with the events from GWTC-3 with  $\text{SNR} \geq 11$  in Fig. A1 (shown in the appendix). The results are consistent with the measurement of the parameters made with events having an  $\text{SNR} \geq 12$ . In this analysis, we have not considered the GW event GW190521 (Abbott et al. 2020a) which has a much higher value of the component masses. The inclusion of such a source leads to a better

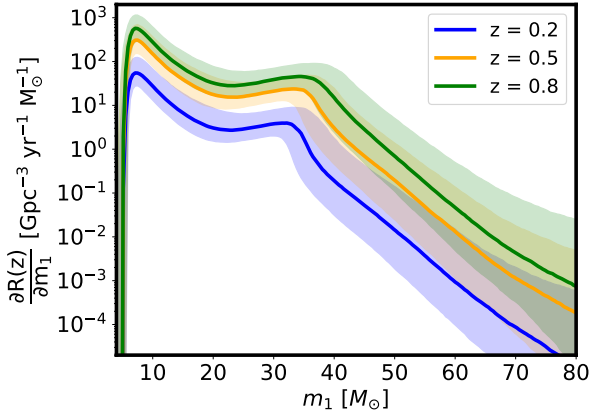


**Figure 11.** BBHs merger rate as a function of redshift for the primary BBHs mass. The different colors indicate the merger rates at different redshifts. Solid lines show the median of the distribution, whereas the shades indicate the 68% CL.

agreement in the value of the Hubble constant as shown in a plot in the appendix (see in Fig. B1). GW sources such as GW190521 are likely to come from a different source population and thus a different theoretical model is necessary to incorporate it.

*Case-2 (GW source population (with fixed  $d = -1$ ) +  $H_0$  parameters):* As in Case-1, we have seen a value of the power-law index significantly away from  $d = -1$  (usually considered as a fiducial value (Fishbach & Kalogera 2021; Mukherjee & Silk 2021)), which is possible for scenarios with flat in log space distribution of the separation between the BHs. Here we perform a joint estimation with the value of the power-law index fixed at  $d = -1$ . The corresponding joint estimations of the parameters are shown in Fig. 6. For this, the merger rate normalization is  $R_0 = 29.55^{+9.85}_{-7.98} \text{ Gpc}^{-3} \text{ yr}^{-1}$ , and the constraints on the minimum delay time  $t_d^{\text{min}}$  have slightly been reduced as shown in the top panel in the orange curve in Fig. 9 (though completely in agreement with the value obtained with  $d$  varying). This happens because, for a scenario with a fixed value of the parameter  $d = -1$ , the peak of the merger rate distribution is shifted towards a lower redshift, as a result by allowing a smaller value of the delay time  $t_d^{\text{min}}$ , the peak of the merger rate position shifts towards a higher redshift. The position of the  $\mu_g$  parameter shows a shift towards a lower value to  $\mu_g = 37.59^{+3.64}_{-3.11} M_\odot$ , as shown in Fig. 9 (bottom, orange curve). Though the posterior is wide and agrees with the fiducial values of the PISN mass scale of  $40 - 60 M_\odot$  (Farmer et al. 2019; Renzo et al. 2020), the maximum a posteriori (MAP) value has shifted to a lower value. So, for a shallower evolution of the merger rate (with  $d = -1$ ), we get a value of  $\mu_g$  in agreement with the previous estimation from GWTC-3 (Abbott et al. 2021b; Virgo & Kagra 2021). However, when estimated jointly with the parameter  $d$ , we find that the value of  $d = -1$  is less supported with respect to other values. Also, in this case, the model fails to capture high mass BHs in comparison to the phenomenological model (Virgo & Kagra 2021), similar to Case-1.

*Case-3 (GW source population parameters with a fixed value of  $H_0$ ):* In this case, we only focus on the GW source population keeping the value of cosmological parameters fixed at the Planck-2018 (Aghanim et al. 2018). The correspond-

ing joint estimations of the parameters are shown in Fig. 7. We find that the value of the  $\mu_g = 40.26^{+2.35}_{-2.32} M_\odot$ , as shown in Fig. 9, has moved to higher values with respect to value allowing  $H_0$  to vary. The value of  $t_d^{\text{min}}$  shows a peak around 2 Gyrs (with about 1 Gyr error-bars at 68% C.I.) and  $d$  are consistent with the case of varying  $H_0$  (see Fig. 9). We also find the value of  $d < -1.55$  for this case. Among all our time delays models, we find that the preferred model is *Case-3*, namely the case in which cosmology is fixed, thus confirming that more events would be needed in order to constrain cosmology and population properties. More interestingly, the *Case-2* model ( $d = -1$ ) is disfavored with respect to *Case-3* and *Case-1* by a factor of  $\sim 1.5$ , which is not enough to claim any statistical evidence but it shows that the value of  $d = -1$  is not supported as the other cases.

## 5 CONCLUSION

The mass, spin, and merger rate of BBHs are a direct probe to infer their formation channels. Though the spin of the BBHs is not yet well inferred from the observations, we can infer the masses and luminosity distance of several BBHs using the network of LIGO/Virgo detectors. The mass distribution and merger rate of the BBHs are likely to exhibit a redshift dependence due to the dependence on metallicity and formation channel of BBHs. In this work, we consider a model which considers the redshift dependence of BBH mass distribution and the merger rate and estimate the parameters of this model from the latest GW catalog of LVK GWTC-3.

By fitting this model with the data with both GW source parameters and cosmological parameters, we show an agreement between the Gaussian peak of the mass distribution with the theoretically expected PISN mass scale. This shows that the Gaussian peak in the mass profile of BHs could likely be reconciled PISN mass-scale value of around  $55 M_\odot$  when time delay information is considered. However, if there exists BHs of second-generation which are going to have masses heavier than predicted by the PISN mass scale, then such systems cannot be captured by this model.

We have found that current data does not favor a model allowing only for first-generation BBH mergers with redshift-dependent mass distribution over the phenomenological redshift-independent mass models. This is due to the high suppression of the production of high mass BBHs, and therefore the necessity of including a model for other formation channels, as well as the increased number of nuisance parameters with respect to the simple phenomenological models. Although a redshift evolution of the BBHs mass distribution can not be confirmed yet, we have shown that (i) a time-delay distribution might play an important role in cosmology, (ii) a time-delay distribution might reconcile the PISN scale with simple phenomenological models and hints towards the formation channels of these BBHs.

In the hypothesis that the BBHs we consider are formed in a stellar binary scenario, we provide an upper limit for the minimum of the time delay distribution. The delay time distribution agrees with the formation channels explored previously. We have also found a value of the power-law index of the delay time distribution  $d < -1$ , which is usually considered as the fiducial value for flat in log space distribution of the spacing between the binaries. The difference in the

value of  $d < -1$  indicates a violation from the standard scenario which exhibits a much steeper merger rate than the scenario with  $d = -1$ . In our analysis, we also jointly infer the value of the Hubble constant, which currently exhibits a large uncertainty and hence is consistent with the value of the Hubble constant inferred from Planck-2018 and SH0ES. However, one of the important parts is that the Hubble constant shows strong degeneracy with the GW source parameters. In particular, in this paper, we have shown that the estimation of the Hubble constant could also be impacted by the BBHs time delay distribution. As a result, if the inferred value of the GW source population is incorrect, then it can bias the value of the Hubble constant and other cosmological parameter estimation.

Though the values of the model parameters considered in this analysis broadly agree with a phenomenological model with no redshift dependence, there are a few key aspects that we have found new in this paper. This model naturally considers a correlation between the merger rate and mass distribution due to the delay time distribution, which naturally leads to both redshift dependence in the merger rate as well as in the mass distribution. The constraints including GW190521 are shown in the appendix. Though the results including GW190521 are consistent with the results without GW190521, one cannot conclude whether GW190521 is from the first generation or the second generation sources. In the future, a revised model including the second-generation BBHs can also be included in the analysis to better understand the population of heavier black holes. Finally, additional sources of uncertainties are likely to arise also from the dependence of the PISN mass scale on the properties of the host galaxy.

In the future with the availability of more sources from the next observation run, a better measurement of the GW source population along with the cosmological parameters will be possible. This will shed light on the formation channels of the binary systems and the redshift dependence of the BH mass distribution.

## ACKNOWLEDGEMENTS

The authors thank Konstantin Leyde for reviewing the manuscript as a part of the LVK review process and for providing useful comments. C. Karathanasis is partially supported by the Spanish MINECO under the grants SEV-2016-0588 and PGC2018-101858-B-I00, some of which include ERDF funds from the European Union. IFAE is partially funded by the CERCA program of the Generalitat de Catalunya. S. Mukherjee is supported by the Simons Foundation. Research at Perimeter Institute is supported in part by the Government of Canada through the Department of Innovation, Science and Economic Development and by the Province of Ontario through the Ministry of Colleges and Universities. S. Mastrogiovanni is supported by the ANR COSMERGE project, grant ANR-20-CE31-001 of the French Agence Nationale de la Recherche. This analysis is carried out at the computing facility of the LSC cluster. We acknowledge the use of following packages in this work: Astropy (Astropy Collaboration et al. 2013, 2018), BILBY (Ashton et al. 2019), Giant-Triangle-Confusogram (Bocquet & Carter 2016), IPython (Pérez & Granger 2007), Matplotlib

(Hunter 2007), NumPy (van der Walt et al. 2011), and SciPy (Jones et al. 01). The authors are grateful for computational resources provided by the LIGO Laboratory and supported by National Science Foundation Grants PHY-0757058 and PHY-0823459. The authors would like to thank the LIGO/Virgo/KAGRA scientific collaboration for providing the data. LIGO is funded by the U.S. National Science Foundation. Virgo is funded by the French Centre National de Recherche Scientifique (CNRS), the Italian Istituto Nazionale della Fisica Nucleare (INFN), and the Dutch Nikhef, with contributions by Polish and Hungarian institutes. This material is based upon work supported by NSF's LIGO Laboratory which is a major facility fully funded by the National Science Foundation.

## DATA AVAILABILITY

The data underlying this article is available on this website <https://www.gw-openscience.org>.

## REFERENCES

- Aasi J., et al., 2015, *Class. Quant. Grav.*, 32, 074001  
 Abbott B. P., et al., 2016a, *Phys. Rev. D*, 93, 112004  
 Abbott B. P., et al., 2016b, *Phys. Rev. Lett.*, 116, 131103  
 Abbott B. P., et al., 2018, *Living Rev. Rel.*, 21, 3  
 Abbott B., et al., 2019a, *Physical Review X*, 9  
 Abbott B. P., et al., 2019b, *The Astrophysical Journal*, 882, L24  
 Abbott R., et al., 2020a, *Phys. Rev. Lett.*, 125, 101102  
 Abbott R., et al., 2020b, *Astrophys. J.*, 896, L44  
 Abbott R., et al., 2021a, *arXiv: 2108.01045*  
 Abbott R., et al., 2021c, *arXiv: 2111.03606*  
 Abbott R., et al., 2021b, *arXiv: 2111.03634*  
 Abbott R., et al., 2021d, *Physical Review X*, 11  
 Abbott B. P., et al., 2021e, *The Astrophysical Journal*, 909, 218  
 Abbott R., et al., 2021f, *The Astrophysical Journal Letters*, 913, L7  
 Acernese F., et al., 2014, *Classical and Quantum Gravity*, 32, 024001  
 Aghanim N., et al., 2018, *arXiv: 1807.06209*  
 Akutsu T., et al., 2020, *arXiv:2005.05574*  
 Arabsalmani M., Sahni V., Saini T. D., 2013, *Phys. Rev. D*, 87, 083001  
 Artale M. C., Mapelli M., Giacobbo N., Sabha N. B., Spera M., Santoliquido F., Bressan A., 2019, *Mon. Not. Roy. Astron. Soc.*, 487, 1675  
 Artale M. C., Mapelli M., Bouffanais Y., Giacobbo N., Spera M., Pasquato M., 2020, *Mon. Not. Roy. Astron. Soc.*, 491, 3419  
 Ashton G., et al., 2019, *Astrophys. J. Suppl.*, 241, 27  
 Aso Y., Michimura Y., Somiya K., Ando M., Miyakawa O., Sekiguchi T., Tatsumi D., Yamamoto H., 2013, *Phys. Rev. D*, 88, 043007  
 Astropy Collaboration et al., 2013, *A&A*, 558, A33  
 Astropy Collaboration et al., 2018, *AJ*, 156, 123  
 Banerjee S., Baumgardt H., Kroupa P., 2010, *MNRAS*, 402, 371  
 Belczynski K., Kalogera V., Bulik T., 2002, *ApJ*, 572, 407  
 Bera S., Rana D., More S., Bose S., 2020, *Astrophys. J.*, 902, 79  
 Bethe H. A., Brown G. E., 1998, *Astrophys. J.*, 506, 780  
 Bocquet S., Carter F. W., 2016, *The Journal of Open Source Software*, 1  
 Buikema A., et al., 2020, *Phys. Rev. D*, 102, 062003  
 Cañas-Herrera G., Contigiani O., Vardanyan V., 2021, *ApJ*, 918, 20  
 Cao L., Lu Y., Zhao Y., 2018, *MNRAS*, 474, 4997

- Cigarrán Díaz C., Mukherjee S., 2022, *MNRAS*, **511**, 2782
- Dayal P., Ferrara A., Dunlop J. S., 2013, *MNRAS*, **430**, 2891
- Del Pozzo W., 2012, *Phys. Rev. D*, **86**, 043011
- Ding X., Biesiada M., Zheng X., Liao K., Li Z., Zhu Z.-H., 2019, *JCAP*, **04**, 033
- Dominik M., Belczynski K., Fryer C., Holz D. E., Berti E., Bulik T., Mandel I., O’Shaughnessy R., 2012, *ApJ*, **759**, 52
- Dominik M., et al., 2015, *Astrophys. J.*, **806**, 263
- Elbert O. D., Bullock J. S., Kaplinghat M., 2018, *Mon. Not. Roy. Astron. Soc.*, **473**, 1186
- Eldridge J. J., Stanway E. R., Tang P. N., 2019, *Mon. Not. Roy. Astron. Soc.*, **482**, 870
- Ezquiaga J. M., Holz D. E., 2022, arXiv:2202.08240
- Farmer R., Renzo M., de Mink S. E., Marchant P., Justham S., 2019, *ApJ*, **887**, 53
- Farr W. M., Fishbach M., Ye J., Holz D., 2019, *Astrophys. J. Lett.*, **883**, L42
- Finke A., Foffa S., Iacovelli F., Maggiore M., Mancarella M., 2021, arXiv:2101.12660
- Fishbach M., Kalogera V., 2021, *Astrophys. J. Lett.*, **914**, L30
- Fishbach M., et al., 2019, *Astrophys. J. Lett.*, **871**, L13
- Fishbach M., et al., 2021, *ApJ*, **912**, 98
- Genel S., 2016, *ApJ*, **822**, 107
- Giacobbo N., Mapelli M., Spera M., 2018, *MNRAS*, **474**, 2959
- Gray R., et al., 2020, *Phys. Rev. D*, **101**, 122001
- Gregory M. H. e. a., 2010, *Classical and Quantum Gravity*, **27**, 084006
- Heger A., Woosley S. E., 2002, *ApJ*, **567**, 532
- Hunter J. D., 2007, *Computing In Science & Engineering*, **9**, 90
- Jones E., Oliphant T., Peterson P., et al., 2001–, SciPy: Open source scientific tools for Python, <http://www.scipy.org/>
- Kimball C., et al., 2021, *Astrophys. J. Lett.*, **915**, L35
- Krumholz M. R., Dekel A., 2012, *ApJ*, **753**, 16
- Lamberts A., Garrison-Kimmel S., Clausen D. R., Hopkins P. F., 2016, *Mon. Not. Roy. Astron. Soc.*, **463**, L31
- Leandro H., Marra V., Sturani R., 2022, *Phys. Rev. D*, **105**, 023523
- Leyde K., Mastrogiovanni S., Steer D. A., Chassande-Mottin E., Karathanasis C., 2022, arXiv:2202.00025
- MacLeod C. L., Hogan C. J., 2008, *Phys. Rev. D*, **77**, 043512
- Madau P., Dickinson M., 2014, *Annual Review of Astronomy and Astrophysics*, **52**, 415–486
- Mancarella M., Genoud-Prachex E., Maggiore M., 2021, arXiv:2112.05728
- Mandel I., de Mink S. E., 2016, *MNRAS*, **458**, 2634
- Mandel I., Farr W. M., Gair J. R., 2019, *Monthly Notices of the Royal Astronomical Society*, **486**, 1086
- Mannucci F., Cresci G., Maiolino R., Marconi A., Gnerucci A., 2010, *MNRAS*, **408**, 2115
- Mapelli M., Giacobbo N., Ripamonti E., Spera M., 2017, *Mon. Not. Roy. Astron. Soc.*, **472**, 2422
- Mastrogiovanni S., et al., 2021a, arXiv:2103.14663
- Mastrogiovanni S., Haegel S., Karathanasis C., Hernandez I. M. n., Steer D. A., 2021b, *JCAP*, **02**, 043
- Mehta A. K., Buonanno A., Gair J., Miller M. C., Farag E., deBoer R. J., Wiescher M., Timmes F. X., 2022, *ApJ*, **924**, 39
- Mukherjee S., 2021, arXiv:2112.10256
- Mukherjee S., Dizgah A. M., 2021, arXiv:2111.13166
- Mukherjee S., Silk J., 2021, *Mon. Not. Roy. Astron. Soc.*, **506**, 3977
- Mukherjee S., Wandelt B. D., 2018, arXiv:1808.06615
- Mukherjee S., Wandelt B. D., Silk J., 2020, *Mon. Not. Roy. Astron. Soc.*, **494**, 1956
- Mukherjee S., Wandelt B. D., Nissanke S. M., Silvestri A., 2021a, *Phys. Rev. D*, **103**, 043520
- Mukherjee S., Wandelt B. D., Silk J., 2021b, *Mon. Not. Roy. Astron. Soc.*, **502**, 1136
- Mukherjee S., Krolewski A., Wandelt B. D., Silk J., 2022, arXiv:2203.03643
- O’Shaughnessy R., Kalogera V., Belczynski K., 2010, *ApJ*, **716**, 615
- Oguri M., 2016, *Phys. Rev. D*, **93**, 083511
- Palmese A., Bom C. R., Mucesh S., Hartley W. G., 2021, arXiv:2111.06445
- Pérez F., Granger B. E., 2007, *Computing in Science and Engineering*, **9**, 21
- Portegies Zwart S. F., Yungelson L. R., 1998, *A&A*, **332**, 173
- Renzo M., Farmer R. J., Justham S., de Mink S. E., Göteborg Y., Marchant P., 2020, *Mon. Not. Roy. Astron. Soc.*, **493**, 4333
- Riess A. G., et al., 2021, arXiv:2112.04510
- Safarzadeh M., Farr W. M., 2019, *ApJ*, **883**, L24
- Santoliquido F., Mapelli M., Giacobbo N., Bouffanais Y., Artale M. C., 2021, *Mon. Not. Roy. Astron. Soc.*, **502**, 4877
- Scelfo G., Boco L., Lapi A., Viel M., 2020, *JCAP*, **10**, 045
- Scelfo G., Spinelli M., Raccanelli A., Boco L., Lapi A., Viel M., 2022, *JCAP*, **01**, 004
- Schutz B. F., 1986, *Nature*, **323**, 310
- Soares-Santos M., et al., 2019, *Astrophys. J. Lett.*, **876**, L7
- Sommariva V., Mannucci F., Cresci G., Maiolino R., Marconi A., Nagao T., Baroni A., Grazian A., 2012, *A&A*, **539**, A136
- Spera M., Mapelli M., 2017, *Mon. Not. Roy. Astron. Soc.*, **470**, 4739
- Taylor S. R., Gair J. R., Mandel I., 2012, *Phys. Rev. D*, **85**, 023535
- Thrane E., Talbot C., 2019, *Publications of the Astronomical Society of Australia*, **36**
- Toffano M., Mapelli M., Giacobbo N., Artale M. C., Ghirlanda G., 2019, *Mon. Not. Roy. Astron. Soc.*, **489**, 4622
- Torrey P., et al., 2019, *MNRAS*, **484**, 5587
- Tse M., et al., 2019, *Phys. Rev. Lett.*, **123**, 231107
- Virgo Kagra 2021, arXiv:2111.03604
- Vitale S., Farr W. M., Ng K., Rodriguez C. L., 2019, *Astrophys. J. Lett.*, **886**, L1
- Vitale S., Gerosa D., Farr W. M., Taylor S. R., 2021, in , *Handbook of Gravitational Wave Astronomy*. Springer Singapore, pp 1–60, doi:10.1007/978-981-15-4702-7\_45-1, [https://doi.org/10.1007/978-981-15-4702-7\\_45-1](https://doi.org/10.1007/978-981-15-4702-7_45-1)
- Ye C., Fishbach M., 2021, *Phys. Rev. D*, **104**, 043507
- You Z.-Q., Zhu X.-J., Ashton G., Thrane E., Zhu Z.-H., 2021, *Astrophys. J.*, **908**, 215
- du Buisson L., et al., 2020, *Mon. Not. Roy. Astron. Soc.*, **499**, 5941
- van der Walt S., Colbert S. C., Varoquaux G., 2011, *Computing in Science and Engineering*, **13**, 22

## APPENDIX A: PARAMETER ESTIMATION WITH A DIFFERENT SNR THRESHOLD.

Here we explore the variation of our results in the case of a lower SNR threshold. In addition to the GW events that we used with  $\text{SNR} \geq 12$  (see Sec. 4), we are now using additionally all events with  $\text{SNR} \geq 11$ . Lowering the SNR causes to run the analysis with 41 events in total. The different posteriors can be seen in Fig. A1. As it can be seen all of the posteriors are in agreement with the  $\text{SNR} \geq 12$  results. The estimations for  $\alpha_{\text{delay}} > 1.81$  and  $\gamma_{\text{delay}} < -1.43$  are very similar to the  $\text{SNR} \geq 12$  ones. We find a delay time power-law index  $d < -1.39$  and a minimum value for the delay time  $t_{\text{d}}^{\text{min}} < 1.94$  Gyrs. The time delay distribution that we find here is less steep than the one of  $\text{SNR} \geq 12$  which leads to a looser constraint for  $t_{\text{d}}^{\text{min}}$  (completely in agreement with the  $\text{SNR} \geq 12$  case though). The value  $d$  is slightly bigger favoring a less steeper increase in the redshift evolution and causing a smaller value of the normalization constant at redshift  $z = 0$   $R_0 = 24.6_{-5.92}^{+7.49} \text{Gpc}^{-3} \text{yr}^{-1}$ . The calculated expected value of

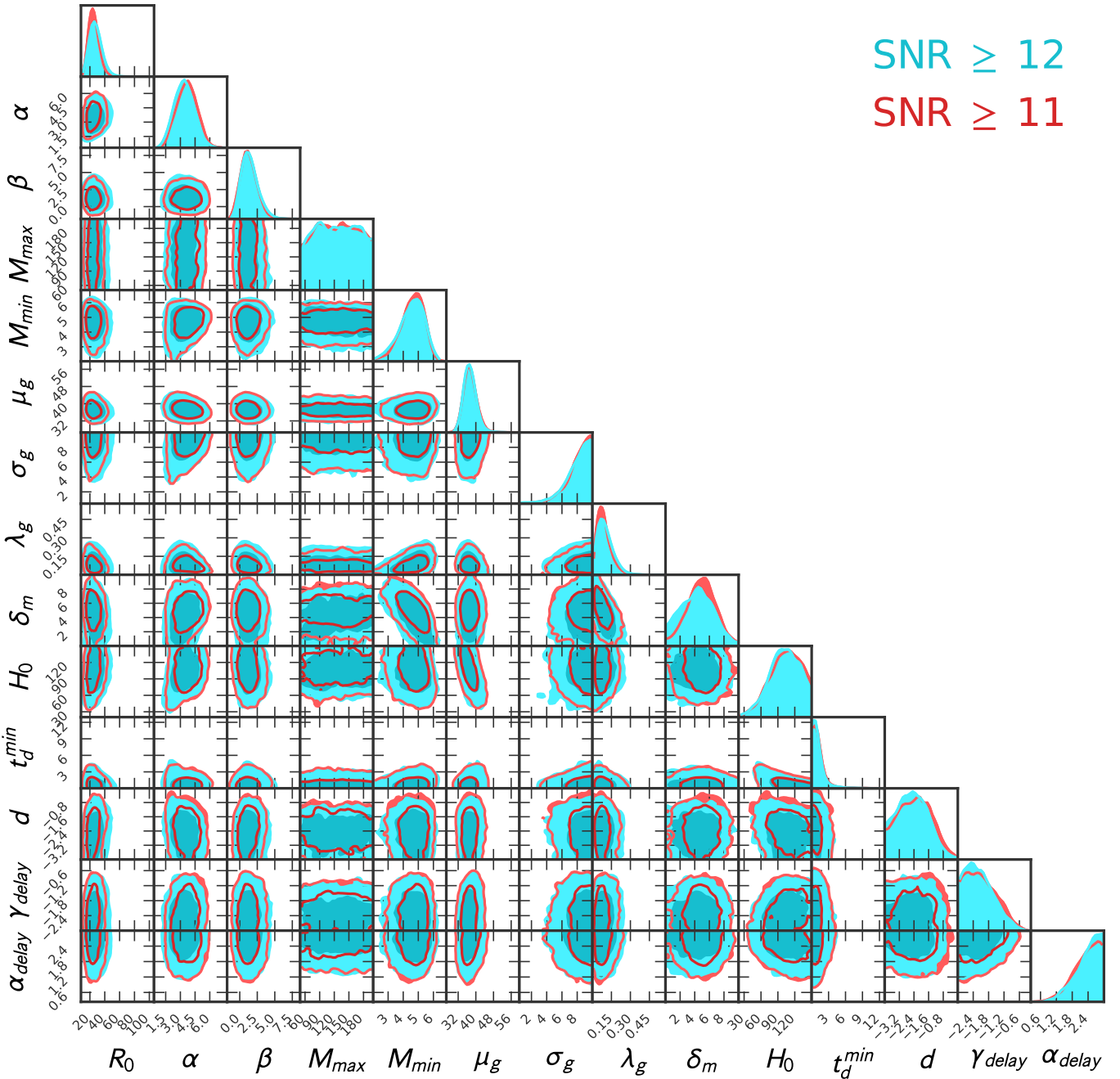


**Figure A1.** Posterior distributions for all the hyper parameters. Here we have fixed all cosmological parameters besides  $H_0$  at their Planck-2018 cosmology. Different posteriors for different SNR thresholds can be seen.

the events is  $N_{\text{exp}} = 41_{-5}^{+6}$  and agrees with the 41 events that were used.

## APPENDIX B: PARAMETER ESTIMATION INCLUDING GW190521

The posteriors of all parameters when including the event GW190521 can be here in Fig. B1. We find a smaller value for the power-law index of the  $m_1$  with  $\alpha = 1.99_{-0.48}^{+0.74}$ , whereas the power-law index of  $m_2$  is very similar  $\beta = 1.28_{-0.93}^{+1.09}$  with

respect to the results that do not include this event. This event has very massive BHs components which cause the power-law index of  $m_1$  to be less steep for the tail of the distribution to be able to account for the very high masses. For the same reason, the estimation for the maximum allowed BHs mass is slightly higher with  $M_{\text{max}} = 138.97_{-39.82}^{+39.81}$   $M_{\odot}$ , but the estimation for the minimum  $M_{\text{min}} = 4.28_{-1.1}^{+1.01}$   $M_{\odot}$  is rather similar. The higher  $M_{\text{max}}$  estimation causes  $H_0$  posterior to move to smaller values (though the posterior is still very wide and in agreement with the results that exclude this event). We find  $H_0 = 82.42_{-32.44}^{+36.85}$  km/s/Mpc and a

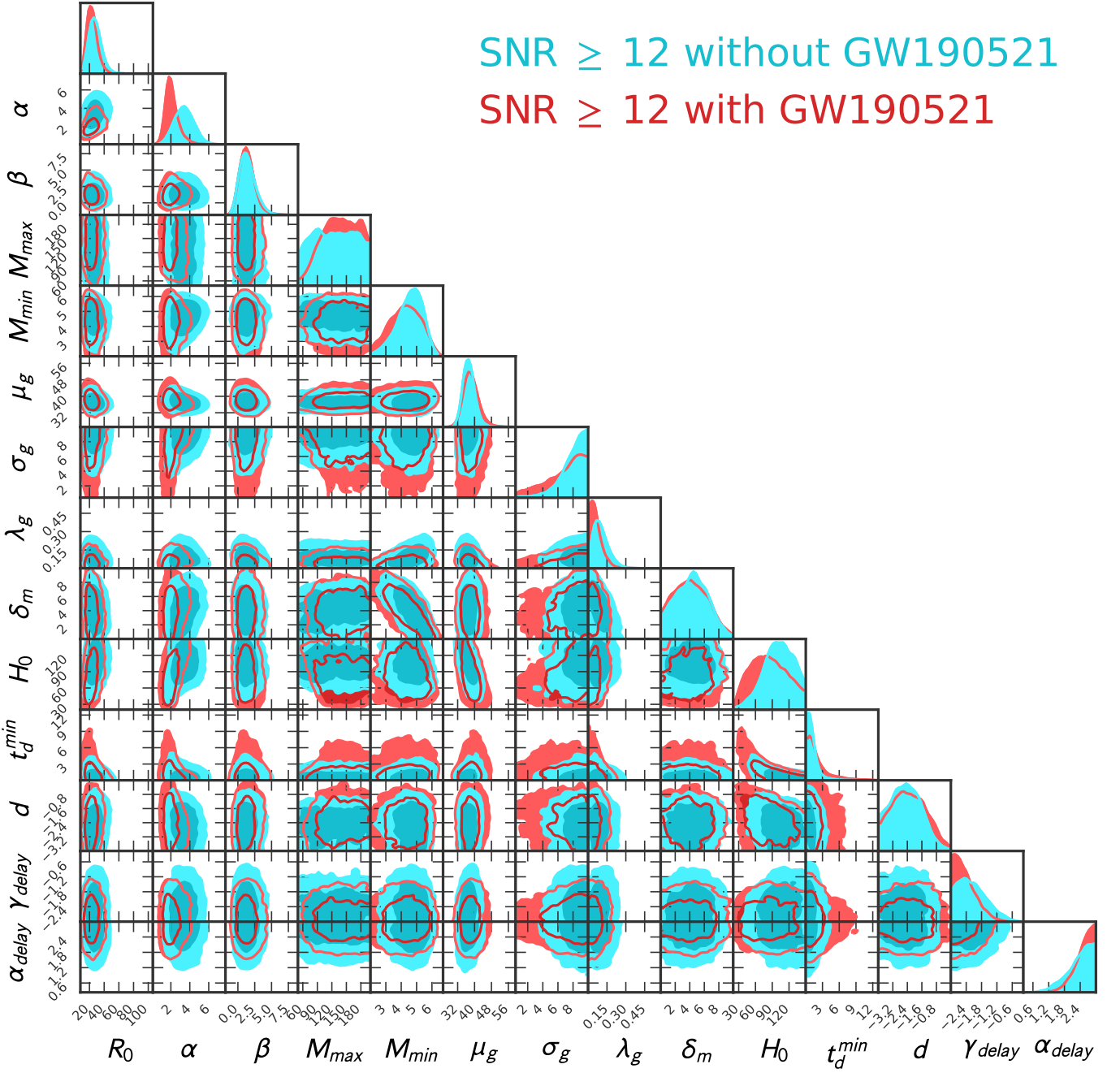


**Figure B1.** Posterior distributions for all the hyper parameters. Here we have fixed all cosmological parameters besides  $H_0$  at their Planck-2018 cosmology. Different posteriors with including or excluding GW190521 can be seen.

rather similar position of the Gaussian peak  $\mu_g = 38.12^{+3.52}_{-2.98} M_\odot$ . We find similar constraints on the index of delay time distribution  $d < -1.30$  but a looser constrain on the minimum delay time  $t_d^{\min} < 3.70$  Gyrs. At redshift  $z = 0$  we find

$R_0 = 23.03^{+7.28}_{-5.94} \text{ Gpc}^{-3}\text{yr}^{-1}$  and estimate that the expected number of events is  $N_{\text{exp}} = 36^{+6}_{-5}$ , which matches with the 35 events used.